JOURNAL OF SOLID STATE CHEMISTRY 118, 323–336 (1995)

Magnetic and Transport Properties of the System $La_{1-x}Sr_xCoO_{3-\delta}$ ($0 < x \leq 0.50$)

M. A. Señarís-Rodríguez and J. B. Goodenough[1]

Center for Materials Science and Engineering, ETC 9.102, University of Texas at Austin, Austin, Texas 78712-1063

Received October 31, 1994; in revised form February 27, 1995; accepted March 2, 1995

Magnetic and transport measurements on the system $La_{1-x}Sr_xCoO_{3-\delta}$ ($0 < x \leq 0.50$, $\delta = 0$ for $0 \leq x < 0.30$, and $\delta(x) \leq 0.06$ for $0.30 \leq x \leq 0.50$) have led to a phase diagram for this system. Upon Sr doping, the material segregates into hole-rich, metallic ferromagnetic regions and a hole-poor matrix similar to $LaCoO_3$. The Co ions of the ferromagnetic phase are in intermediate-spin configurations; the hole-poor matrix experiences a thermally induced low-spin to high-spin transition. For low Sr doping ($x < 0.20$), the hole-rich regions are isolated from one another and show superparamagnetic behavior below $T_c \approx 240$ K; long-range magnetic order via frustrated intercluster interactions occurs below a superparamagnetic freezing temperature T_g that increases with x. At $x = 0.20$, the coupling between the intermediate-spin, metallic ferromagnetic clusters wtihin an interpenetrating matrix reaches a magnetic percolation threshold that orders the clusters ferromagnetically below $T_c \approx 250$ K. However, the electrical conduction in the ferromagnetic regions is modulated by the matrix, which has a spin state that varies with temperature. This causes a reentrant semiconductive behavior in the samples with $0.20 \leq x \leq 0.25$. Metallic ferromagnetic behavior is found for $0.30 \leq x \leq 0.50$ even though the presence of an interpenetrating hole-poor matrix persists to $x = 0.50$. A ferromagnetic fraction less than unity leads to peculiar magnetic properties that have been attributed in the literature to a magnetic "cluster glass."

INTRODUCTION

$LaCoO_3$ and other rare-earth cobaltates are of interest because of the peculiar way their magnetic and transport properties change with temperature (1–6). To explain this behavior, early work on $LaCoO_3$ established the existence of a thermally induced spin transition from low-spin Co(III) to mostly high-spin Co^{3+} (3). Since then, many investigations have been carried out in order to elucidate how this spin transition takes place and how the material evolves from a semiconducting to a metallic behavior as the temperature increases (7–12). We have recently proposed a revised model for $LaCoO_3$ that appears to resolve the outstanding questions concerning the character of the transition with increasing temperature in this compound (12).

Substitution of Sr^{2+} for La^{3+} in $LaCoO_3$ brings about remarkable changes in the system (13–16); while $LaCoO_3$ shows high resistivity and antiferromagnetic exchange interactions, the $La_{1-x}Sr_xCoO_{3-\delta}$ materials evolve toward a ferromagnetic intermediate-spin state with itinerant σ^* electrons as x increases (17). Bahadur *et al.* (18) reported Mössbauer data supporting an intermediate-spin state for the ferromagnetic regions of their samples. Thus, according to the early literature, the $x = 0.5$ composition is a good conductor ($\rho < 10^{-4}$ Ω-cm) and has a metallic temperature coefficient; in addition, it is a ferromagnet with a moment of approximately 1.5 μ_B per formula unit (13, 14).

Early studies led to the suggestion that, in the doped samples, paramagnetic La^{3+} regions coexist with ferromagnetic Sr^{2+}-rich clusters in the same crystallographic phase, the ferromagnetic component increasing with x (14).

We have reexamined the structural, magnetic, and transport behavior of the $La_{1-x}Sr_xCoO_{3-\delta}$ system in order to investigate the evolution of its properties upon doping and the variation of the spin state at the cobalt ions with composition and temperature. In the course of our investigations, other studies of the magnetic properties of this system have been reported in the literature (19, 20). Our transport data supplement the magnetic data and allow a more detailed phase diagram for this system.

EXPERIMENTAL

$La_{1-x}Sr_xCoO_{3-\delta}$ samples ($0 < x \leq 0.36$) were prepared by a coprecipitation method from La_2O_3, $Co(NO_3)_2 \cdot 6H_2O$ and $SrCO_3$ as starting materials. The cobalt nitrate was first dissolved in water; the cobalt content in the solution was determined gravimetrically with anthranilic acid as the precipitating agent. Known volumes of this cobalt solution were then mixed with the corresponding lanthanum and strontium nitrate solutions obtained by

[1] To whom correspondence should be addressed.

0022-4596/95 $12.00

dissolving in nitric acid weighted amounts of dry La_2O_3 and $SrCO_3$. Coprecipitation at pH 11 was achieved by adding aqueous solutions of KOH and K_2CO_3 as precipitating agents. The precipitates were carefully washed, dried, and then decomposed at 750°C.

In order to retain a high oxidation state, samples of $La_{1-x}Sr_xCoO_{3-\delta}$ ($0.36 < x \leq 0.50$) were prepared as follows. Stoichiometric amounts of dry La_2O_3 and $SrCO_3$ were dissolved in nitric acid; they were then mixed with the appropriate volume of the cobalt nitrate solution previously described. The obtained solution was gently heated so that a slow evaporation of the solvent took place. The resulting mixture of nitrates was decomposed at 600°C.

The precursor powders obtained by both routes were subsequently pressed into pellets, heated in air at 1000°C for 77 h, and cooled slowly to room temperature (1°/min).

The product materials were examined by X-ray powder diffraction with a Philips PW 1729 diffractometer and $CuK_\alpha = 1.5418$ Å radiation. NaCl was used as an internal standard. The thermal stability of all the materials was checked by differential thermal analysis (DTA) and thermogravimetric analysis (TGA) with a Perkin–Elmer Thermal Analysis system. Iodometric titrations were carried out to analyze the oxygen content of the materials: the samples were dissolved in acidified KI solutions, and the I_2 generated was titrated against a thiosulphate solution; the whole process was carried out under a nitrogen atmosphere.

Electron diffraction studies were carried out on two samples with intermediate Sr content ($x = 0.15$ and 0.30) in a Jeol 2000 FX microscope working at 200 KeV.

Magnetic properties of sintered pellets were studied in a Quantum Design MPMS SQUID magnetometer; zero-field-cooled (ZFC) and field-cooled (FC) magnetic susceptibility measurements were obtained in fields $10 \leq H \leq 1000$ Oe from 4.2 to 380 K and in fields $1000 \leq H \leq 5000$ Oe from 380 to 750 K. ZFC magnetization curves $M(H)$ were obtained at 5 K and at temperatures slightly below and above the temperature of long-range magnetic order; to do these measurements, the samples were first heated to 340 K and then cooled in zero field to the specified temperature. Then, the magnetic field was switched on and varied up to ±50 kOe.

The electrical resistance of pressed pellets was measured in the range $15 \leq T \leq 823$ K in a home-made four-probe device equipped with a Lakeshore temperature controller.

Seebeck coefficients of pressed pellets were measured in the temperature interval $15 \leq T \leq 823$ K with a home-made device described elsewhere (21).

Electrical resistance measurements under nearly hydrostatic pressure were performed with a Be–Cu self-clamping device (22) containing a Teflon cell, a lead manometer, and a 1:1 mixture of *n*-pentane and isoamyl alcohol as a pressure-transmitting medium. The applied pressures ranged between 1 bar $\leq P \leq 12$ kbar. Thin copper wire pressed to the sample's surface made contact via small pieces of indium foil. The sample temperature was measured with a silicon diode attached to a place near the Teflon cell. During a measuring run, the cooling rate was computer-controlled to be less than 0.1 K/min.

RESULTS

1. Sample Characterization

According to the room-temperature X-ray diffraction results, the obtained $La_{1-x}Sr_xCoO_{3-\delta}$ samples ($0 < x \leq 0.50$) were single-phase materials. Also, the introduction of the larger size Sr^{2+} cation progressively reduces the rhombohedral distortion present in the parent $LaCoO_3$ compound; for $x = 0.5$ the crystal symmetry is almost cubic. The lattice parameters calculated from the X-ray diffraction patterns are in good agreement with those reported in the literature (14, 15).

As in our recent results on $LaCoO_3$ (12), differential thermal analysis did not show the endothermic peak at ~1200 K reported in the early literature (14, 15), which was due to an undetected Co_3O_4 impurity.

The thermogravimetric results show that for lower Sr content ($x \leq 0.20$), the samples lose some oxygen on heating above 923 K, but they recuperate it on slow cooling in air so that the oxygen stoichiometry is preserved below 773 K. For $x > 0.25$, the oxygen loss on heating is more pronounced; although some is recuperated on cooling, the oxygen content of these samples is different for heating and cooling runs above room temperature.

The iodometric titrations reveal that while as-prepared samples with Sr content $x \leq 0.25$ are stoichiometric in oxygen ($La_{1-x}Sr_xCoO_{3.00\pm0.01}$), the samples with $x > 0.25$ are oxygen deficient. From these analyses, the chemical compositions of the more highly doped samples are $La_{0.70}Sr_{0.30}CoO_{2.99\pm0.01}$, $La_{0.64}Sr_{0.36}CoO_{2.97\pm0.01}$, and $La_{1-x}Sr_xCoO_{2.94\pm0.01}$ ($0.40 \leq x \leq 0.50$).

Two samples with intermediate Sr content ($x = 0.15$ and 0.30) were studied by means of electron diffraction in a search for any possible segregation and/or ordering between the La^{3+} and Sr^{2+} cations. No superstructure spots were detected in any of the various microcrystals selected and orientated along different zone axes; only a change from rhombohedral to almost tetragonal symmetry was observed as the Sr content increased.

2. Magnetic and Transport Properties

In view of their different magnetic and transport properties, we distinguish two groups of samples in the

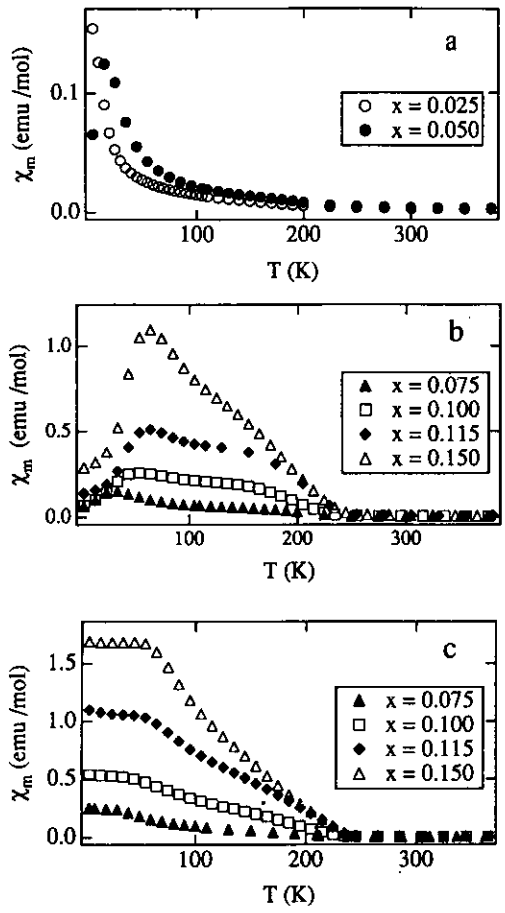

FIG. 1. Temperature dependence of the molar magnetic susceptibility of $La_{1-x}Sr_xCoO_3$ samples in the temperature interval 4.2 K $\leq T \leq$ 380 K, measured in a field of 1 kOe. (a) $0.025 \leq x \leq 0.050$ (ZFC measurements). (b) $0 < x \leq 0.150$ (ZFC results). (c) $0 < x \leq 0.150$ (FC results).

$La_{1-x}Sr_xCoO_{3-\delta}$ system: samples with (a) $0 < x \leq 0.15$, and (b) $0.20 \leq x \leq 0.50$.

Magnetic Properties

(a) $0 < x \leq 0.15$. The temperature dependence of the molar magentic susceptibility of samples $0 < x \leq 0.150$, $\chi_m(T)$, was measured in fields $H = 1$ kOe on heating from low temperature after cooling in zero magnetic field (ZFC case) or in a field of 1 kOe (FC-1 kOe case). Figure 1 shows typical $\chi_m(T)$ curves for these samples. From these curves we note several features and distinguish two critical temperatures.

(1) A marked increase in $\chi_m(T)$ occurs below a $T_c \approx$ 240 K, which marks the onset of magnetic order within superparamagnetic clusters. Evidence for superparamagnetism is already seen at x = 0.025, Fig. 1(a), and extends over the entire range $0.025 \leq x \leq 0.15$, Fig. 1(b), (c).

(2) A sharp maximum in the ZFC $\chi_m(T)$ curve at a transition temperature $T_g < T_c$ increases from 15 K at $x = 0.050$ to 65 K at $x = 0.15$ (Figs. 1a and 1b). In the FC-1 kOe samples, $\chi_m(T)$ is nearly temperature-independent below T_g, (Fig. 1c); significantly, T_g is lowered by cooling in larger magnetic fields.

These results, which are indicative of a spin-blocking behavior due to magnetic interactions between superparamagnetic clusters, are in excellent agreement with the ones found by Itoh *et al.* (18), who used a measuring field $H = 20$ Oe. However, it should be noted that for a superparamagnetic blocking at temperatures $T \leq T_g$, the meaningful parameter is the magnetization M, not χ_m, as M is no longer proportional to H at $T \leq T_g$. In our measurements, $M = \chi_m H$ with $H = 1$ kOe.

Figure 2 provides further evidence of spin-blocking behavior below T_g. At 5 K the M versus H curve of the ZFC sample shows no saturation at 50 kOe; lack of saturation in high fields is a characteristic feature of spin glasses (23). Moreover, Itoh *et al.* (19) have shown an aging effect in the magnetization of ZFC samples, which is another characteristic feature of spin glasses. Finally, a recent neutron-diffraction study on a sample $x = 0.080$ has provided more direct evidence for a blocking of the superparamagnetic spins (20).

Another notable feature of Fig. 1 is the appearance of a shoulder in the $\chi_m(T)$ curves near 150 K for $0.050 \leq x \leq 0.15$.

The plots of $\chi_m^{-1}(T)$ shown in Fig. 3 are also instructive. The curve for $LaCoO_3$ has a plateau in the interval $400 < T < 650$ K, separating the two Curie–Weiss temperature domains in which the ratio of high-spin Co^{3+} to

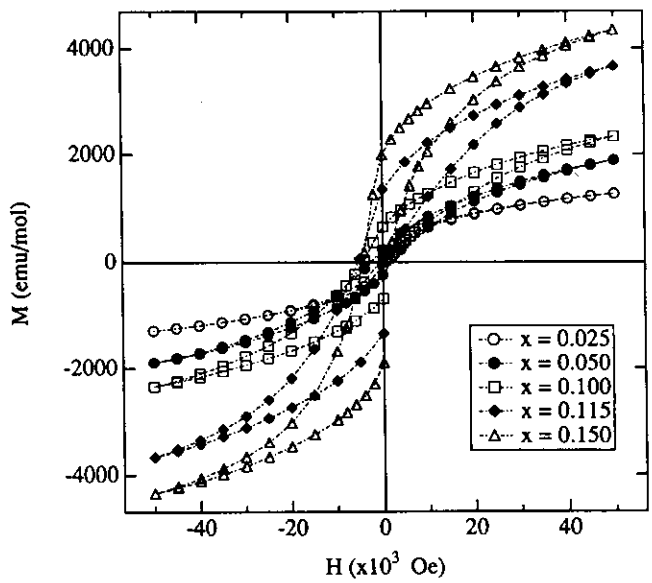

FIG. 2. ZFC magnetization M versus applied field H of $La_{1-x}Sr_xCoO_3$ ($0 < x \leq 0.15$) at 5 K.

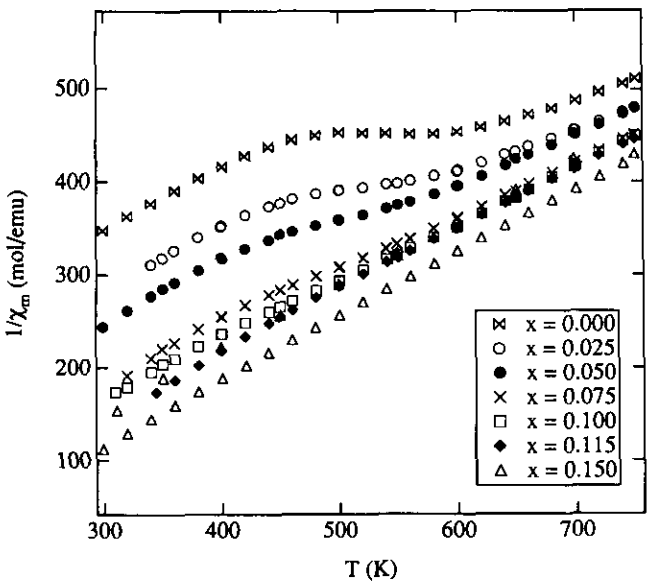

FIG. 3. Inverse molar magnetic susceptibility versus temperature for $La_{1-x}So_xCoO_3$ ($0 \leq x \leq 0.15$) in the temperature range 310 K $\leq T \leq$ 750 K (H = 5000 Oe). The curve corresponding to $LaCoO_3$ is shown as a reference.

total cobalt remains nearly constant (12). Although the appearance of superparamagnetic clusters below T_c causes the plateau in $\chi_m^{-1}(T)$ to fade with increasing x over the interval $0.025 \leq x \leq 0.10$, a fit to the Curie–Weiss law in the two temperature domains $T_c < T < 350$ K and $T > 650$ K provides an indicator of how the effective mean atomic moment per cobalt ion, μ_{eff}, and the mean interatomic exchange interactions, as expressed by the Weiss constant θ, are evolving with x. As shown in Fig. 4, such curve fitting gives a μ_{eff} that decreases slowly with x and a θ that increases from negative to positive values with increasing x for both temperature intervals.

(b) 0.20 ≤ x ≤ 0.50. Samples with higher Sr doping ($x \geq 0.20$) show a large magnetization $M = \chi_m H$ setting in below T_c, Fig. 5; long-range magnetic order occurs at T_c rather than at a $T_g \leq T_c$, and it gives a net magnetization as in a ferromagnet. The transition temperature $T_c \approx 250$ K at $x = 0.20$ increases only slowly with x to a $T_c \approx 255$ K at $x = 0.50$; a T_c independent of x would have indicated disproportionation into two phases.

Over the temperature interval $T_c < T < 750$ K, the Curie–Weiss $\chi_m(T)$ curves for samples $x \geq 0.25$ have a $\theta \geq T_c$ as in a normal ferromagnet whereas for $x \leq 0.15$ the Weiss constant is $\theta < T_c$.

Figure 6 shows the M versus H curves at 5 K for samples $0.20 \leq x \leq 0.50$. The hysteresis loops approach a saturation of M at 50 kOe with much smaller coercive fields than the $M(H)$ curves of Fig. 2; however, they show a relatively small remanence. Moreover, a weak hysteresis is observed in the M versus H experiments performed near but above T_c. Similar anomalies in the B–H behavior have been reported by Menyuk *et al.* (24) for the case of $x = 0.50$. Although saturation is not completely achieved, we calculate a mean ferromagnetic moment per cobalt ion $\mu_{Co} = n_n \mu_B$ by extrapolating the $M(H)$ for $25 \leq H \leq 50$ kOe back to $H = 0$; these values are given in Table 1 together with the values of μ_{eff} and θ obtained from the Curie–Weiss law for $T > T_c$. Comparison of the values of n_b at 5 K with the μ_{eff} so obtained shows clearly that the number of unpaired spins is larger at higher temperatures. The FC-H curves of χ_m versus T in Fig. 5b show an unusual shape below T_c, which suggests that the ferromagnetic behavior is anomalous.

Transport Properties

Measurements of thermoelectric power versus temperature, $\alpha(T)$, are shown in Figs. 7 and 8 for $0 < x \leq 0.150$.

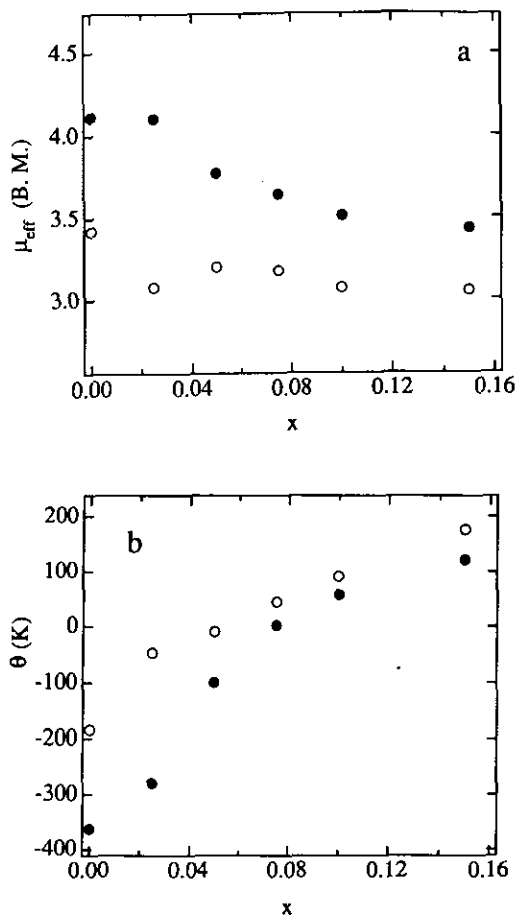

FIG. 4. (a) Effective magnetic moment, μ_{eff}, of $La_{1-x}Sr_xCoO_3$ ($0 < x \leq 0.15$) corresponding to the temperature interval 150 K $< T <$ 350 K (results from the ZFC experiments) (○) and to $T <$ 650 K (●). (b) Weiss constant, θ, of $La_{1-x}Sr_xCoO_3$ ($0 < x \leq 0.15$) corresponding to the temperature interval $150 < T < 350$ K (results from the ZFC experiments) (○) and to $T >$ 650 K (●).

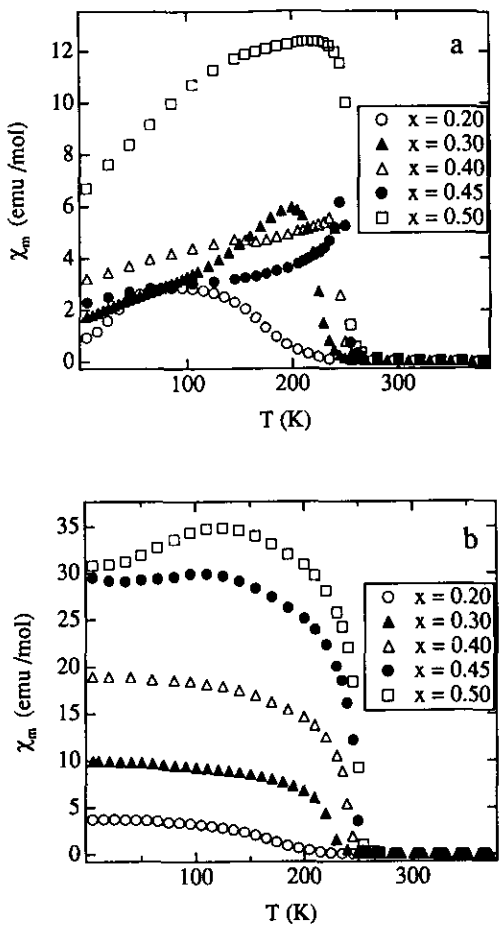

FIG. 5. (a) FC and (b) FC molar magnetic susceptibility of $La_{1-x}Sr_xCoO_{3-\delta}$ ($x \geq 0.20$) in the temperature interval 4.2 K $\leq T \leq$ 380 K. The samples have been measured in the following fields: 400 Oe ($0.20 \leq x \leq 0.30$) and 20 Oe ($0.40 \leq x \leq 0.50$).

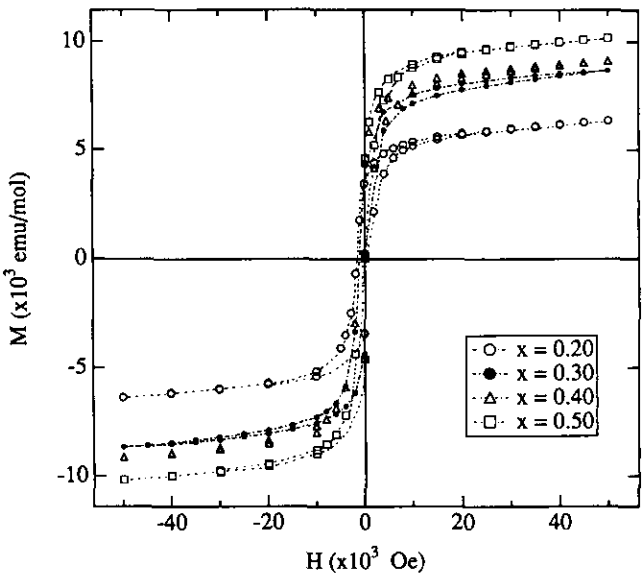

FIG. 6. ZFC magnetization M versus applied field H of $La_{1-x}Sr_xCoO_{3-\delta}$ ($0.20 \leq x \leq 0.50$) measured at 5 K.

They allow us to define two additional critical temperatures, T_s and T_s', that mark the upper and lower temperatures of a plateau in the $\alpha(T)$ curve. The plateau is well-defined in the compositional range $0 < x \leq 0.050$; it signals a temperature range in which electrical conduction is dominated by small-polaron holes of nearly constant concentration. This range corresponds to the temperature interval $110 < T < 350$ K over which the magnetic susceptibility χ_m of $LaCoO_3$ has a nearly Curie–Weiss temperature dependence below the plateau in the χ_m^{-1} versus T curve of Fig. 3. The plateau in $\alpha(T)$ is less well-defined in the compositional range $0.075 \leq x \leq 0.150$, where $\alpha(T)$ begins to diminish smoothly with temperature above about 240 K, which corresponds to T_c.

Above T_s, the $\alpha(T)$ curve decreases rapidly, especially at lower x, with increasing temperature until a new semiconductive state is reached at a T_v.

The $\alpha(T)$ curves below 300 K for the more highly doped samples $0.20 \leq x \leq 0.50$ are shown in Fig. 9. In samples $x \geq 0.30$, $\alpha(T)$ is negative within the ferromagnetic temperature domain, but rises to a small positive value at higher temperatures. At room temperature, the magnitude of α decreases monotonically with increasing x to a small value typical of a metal.

Figure 10 shows a high-temperature $\alpha(T)$ curve for $x = 0.25$. Although α remains positive to 823 K, it decreases smoothly with increasing temperature, which is not characteristic of a simple metal. On cooling, the $\alpha(T)$ curve was a little larger because of some loss of oxygen at higher temperatures.

Attempts to investigate the transport properties at temperatures $T > 300$ K for $0.30 \leq x \leq 0.50$ were frustrated by an irreversibility of the heating and cooling curves due to loss of oxygen from the samples at higher temperatures.

Samples with $0 < x \leq 0.15$ were all semiconductive to above 800 K. Resistance data for $x = 0.050$ are shown in Fig. 11. In the range $110 < T < 310$ K where the $\alpha(T)$

TABLE 1

Effective Magnetic Moment, μ_{eff}, and Weiss Constant, θ, of $La_{1-x}Sr_xCoO_{3-\delta}$ ($0.20 \leq x \leq 0.50$) Calculated for $T > T_c$, Together with the Corresponding Magnetic Moment per Co Ion, n_b, at 5 K

x	μ_{eff}/μ_B	θ(K)	n_b
0.20	3.35	182	0.97
0.25	3.39	217	1.26
0.30	3.48	239	1.39
0.40	3.41	242	1.46
0.45	3.67	251	1.51
0.50	3.85	252	1.62

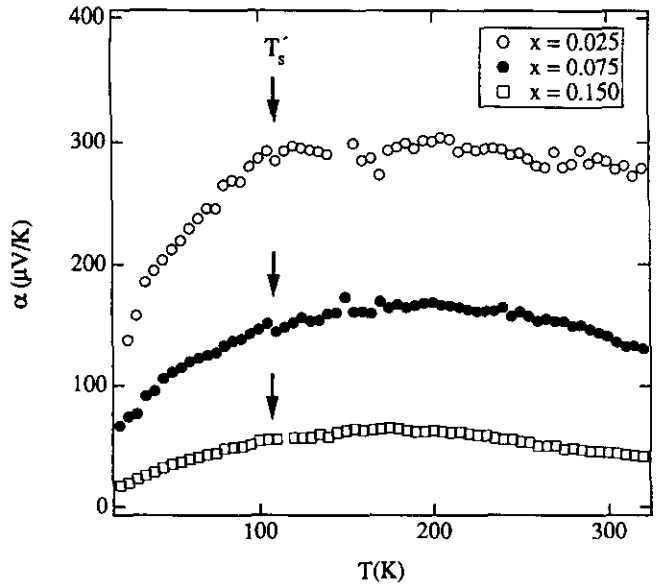

FIG. 7. Temperature dependence of the Seebeck coefficient of $La_{1-x}Sr_xCoO_3$ ($0 < x \leq 0.15$) in the temperature interval 15 K $< T <$ 310 K.

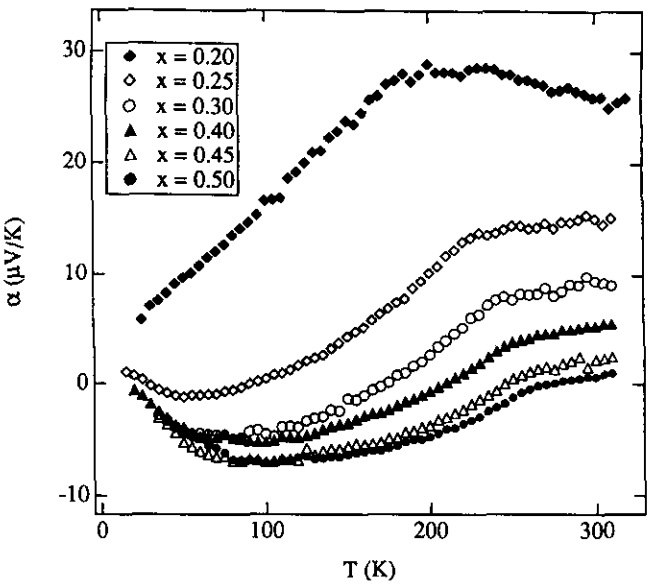

FIG. 9. Temperature dependence of the Seebeck coefficient of $La_{1-x}Sr_xCoO_3$ ($0.25\ x \leq 0.50$) in the temperature interval 15 K $< T <$ 310 K.

curves indicate the conduction is by small-polaron holes, we may obtain an activation energy from the slope of the ln (T/R) versus T^{-1} curve of Fig. 12a; we use the conductivity expression

$$\sigma = pe\mu_p \sim T^{-1} \exp(-E_a/kT), \qquad [1]$$

where the mobility of a small-polaron hole is

$$\mu_p = \frac{eD_o}{kT} \exp(-\Delta G_m/kT) \qquad [2]$$

with a motional free energy $\Delta G_m = \Delta H_m - T\Delta S_m$.

Trapping of the holes at Sr^{2+} ions by an energy ΔH_t may occur at low temperatures, but a $d(\Delta H_t)/dx < 0$ can be expected below the percolation threshold for cobalt sites near neighbor to a Sr^{2+} ion. Addition of a ΔH_t makes

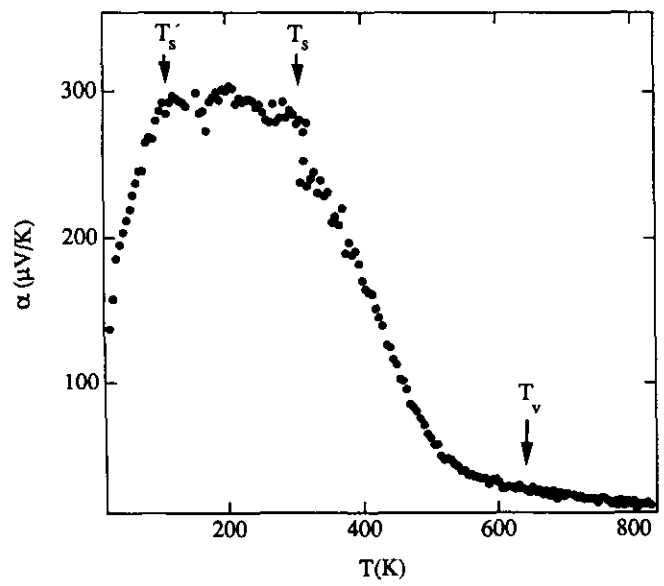

FIG. 8. Temperature dependence of the Seebeck coefficient of $La_{0.95}Sr_{0.050}CoO_3$ in the temperature interval 15 K $\leq T \leq$ 823 K.

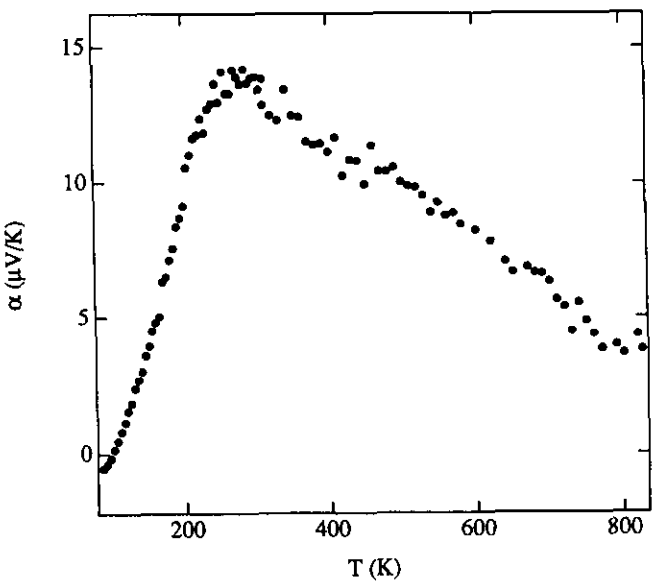

FIG. 10. Temperature dependence of the Seebeck coefficient of $La_{0.75}Sr_{0.25}CoO_3$ in the temperature interval 15 K $\leq T \leq$ 823 K.

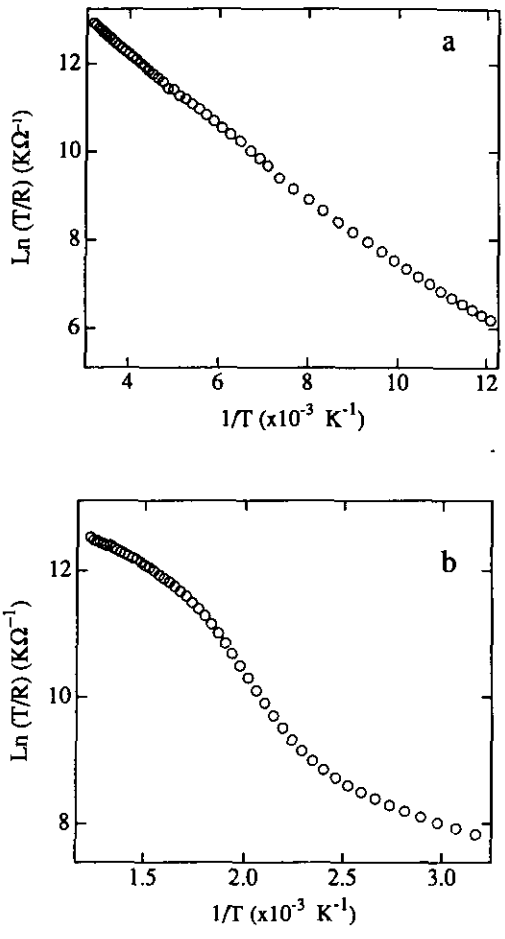

FIG. 11. Plots of $\ln(T/R)$ versus T^{-1} for $La_{0.95}Sr_{0.050}CoO_3$. (a) low-temperature interval: 80 K $\leq T \leq$ 310 K. (b) high-temperature interval: 300 K $\leq T \leq$ 823 K.

$$E_a = \Delta H_m + (1/2)\,\Delta H_t. \qquad [3]$$

At lowest temperatures where most of the cobalt are in a low-spin state, the activation energy is somewhat smaller than in the interval $T_s' < T < T_s$, where the ratio of high-spin to low-spin cobalt remains approximately constant. The measured E_a ($T > T_s'$) decreases from 0.08 eV for $x = 0.025$ to 0.04 eV for $x = 0.150$, which suggests a $\Delta H_t < 0.1$ eV.

In the range $T_s < T < T_v$, the resistance drops sharply with increasing temperature, (Fig. 11b); this drop signals an important change is taking place in the character of the conducting holes. Above T_v, a new semiconductive state is stabilized; it has a mobile hole concentration $p \gg x$ and a very small activation energy.

Samples with $0.30 \leq x \leq 0.50$ were all metallic, but they exhibited a change of slope at T_c as a result of spin-disorder scattering; see Fig. 12 for $x = 0.45$. The influence of spin-disorder scattering has been clearly demonstrated for ferromagnetic CrO_2 (25). The metallic samples were all oxygen-deficient.

Samples in the range $0.20 \leq x < 0.30$ exhibited a metallic temperature dependence in a temperature interval below T_c, but semiconductive behavior outside this interval; see Fig. 13. The transition temperatures at the bottom and top of this interval are designated T_{MI}.

Figure 14 shows the change in the electrical resistance curves $R(T)$ with hydrostatic pressure for samples $x = 0.25$, 0.30, 0.45. Since the slope of the $R(T)$ curves changes at T_c in the metallic samples, it is possible to monitor the pressure dependence of T_c. The $x = 0.25$ sample shows a $dR/dP > 0$ for all temperatures $T < 300$ K and $dT_c/dP \approx 0$. The $x = 0.30$ sample had a $dR/dP \approx dT_c/dP \approx 0$. The $x = 0.45$ samples shows a $dR/dP < 0$ until $P = 9.1$ kbar; $R(T)$ increases between 9.1 and 10.3 kbar, but decreases again above 10.3 kbar. A $dT_c/dP > 0$ is found for $P > 9.1$ kbar; T_c reaches a saturation value for $P \geq 9.1$ kbar.

DISCUSSION

Figure 15 gives the phase diagram obtained from the magnetic and electrical data for the system $La_{1-x}Sr_xCoO_{3-\delta}$; it contains one critical composition, x_m, as well as the several critical temperatures T_g, T_c, T_s', T_s, T_{MI}, and T_v that were identified in the data presentation. The diagram is complex despite a structural evolution indicating a complete solid solution in a single crystallographic phase at room temperature. The complexity arises

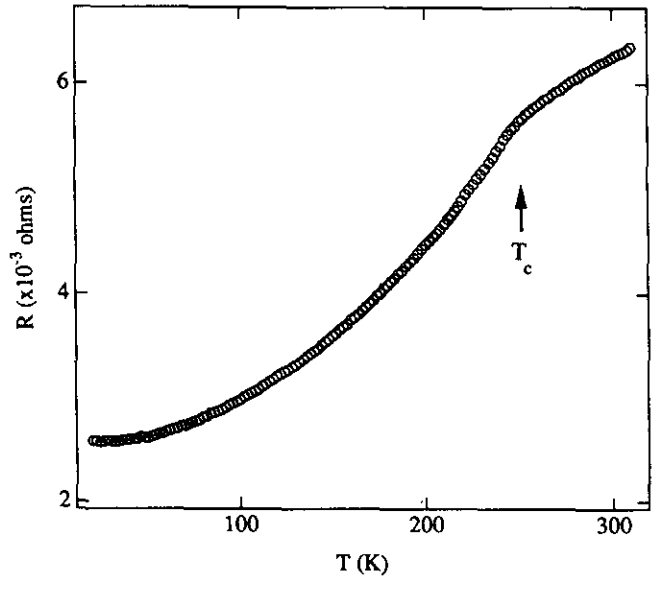

FIG. 12. Variation with temperature of the electrical resistance of $La_{0.65}Sr_{0.45}CoO_{2.96}$. All samples $La_{1-x}Sr_xCoO_{3-\delta}$, $0.30 \leq x \leq 0.50$, show a similar behavior.

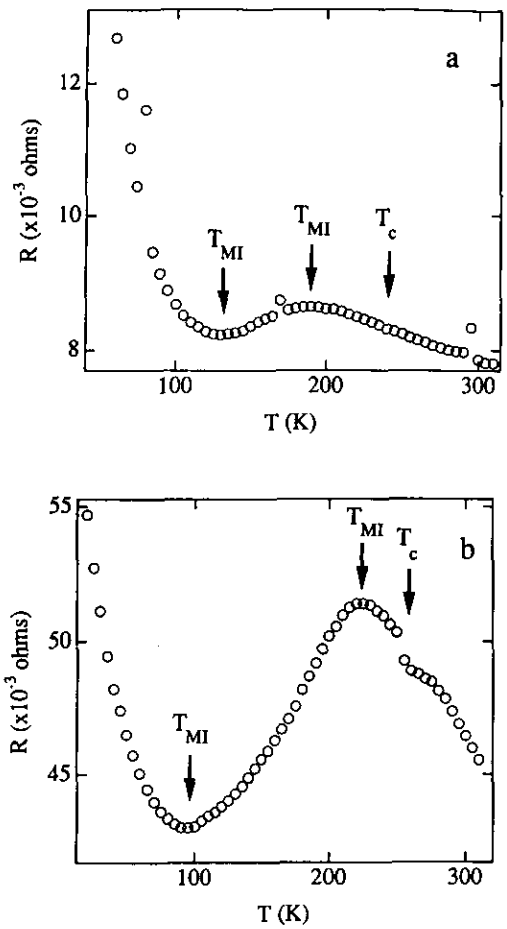

FIG. 13. Variation with temperature of the electrical resistance of (a) $La_{0.80}Sr_{0.20}CoO_3$ and (b) $La_{0.75}Sr_{0.25}CoO_3$ in the temperature interval 15 K $\leq T \leq$ 310 K.

from three factors: a trapping of the Co(IV) at Sr^{2+} ions, a change with temperature and doping in the spin confiuration of trivalent cobalt, and the coexistence of localized π-antibonding t_2 electrons and σ-antibonding e electrons that evolve from localized to itinerant character with changes in the e electron concentration.

Our interpretation of Fig. 15 begins with a review of the properties of the parent composition $LaCoO_3$ that have already been established (12). The bulk trivalent cobalt ions of $LaCoO_3$ all have low-spin Co(III): $t_2^6e^0$ configurations at T = 0 K that transform with increasing temperature toward a uniform nearly high-spin $t_2^{(5-y)}\sigma^{*(1+y)}$, $y \geq 0.5$, configuration at temperatures $T > 650$ K. (We use σ^* to denote itinerant σ-antibonding states of e orbital parentage). With increasing temperature, this evolution occurs in the following steps:

(1) Below T_{on} = 35 K, $LaCoO_3$ is an insulator and all the bulk cobalt are low-spin Co(III); but some high-spin Co^{3+}: $t_2^4e^2$ configurations at the surface or associated with lattice defects give a contribution to χ_m.

(2) In the interval 35 K $< T <$ 110 K, i.e., $T_{on} < T < T_s'$, high-spin Co^{3+} ions are progressively created; the smaller covalent bonding to a high-spin Co^{3+} ion stabilizes low-spin Co(III) on the near-neighbor cobalt atoms via the inductive effect, so the Co^{3+} : Co(III) ratio remains under 50 : 50.

(3) Between 110 and 350 K, i.e., $T_s' < T < T_s$, a dynamic ordering between the high-spin and low-spin ions stabilizes a population near 50 : 50 Co^{3+} : Co(III), which results in a Curie–Weiss behavior of the χ_m^{-1} versus T curve. The Seebeck coefficient $\alpha(T)$ is positive and large; a small $d\alpha/dT < 0$ reflects the excitations of mobile charge carriers across a band gap in the compound in this temperature range.

(4) In the interval 350 $< T <$ 650 K, i.e., $T_s < T < T_v$, where the χ_m^{-1} versus T curve of Fig. 3 shows a plateau, the remaining low-spin Co(III) are transformed progressively to the intermediate-spin configuration Co(iii):

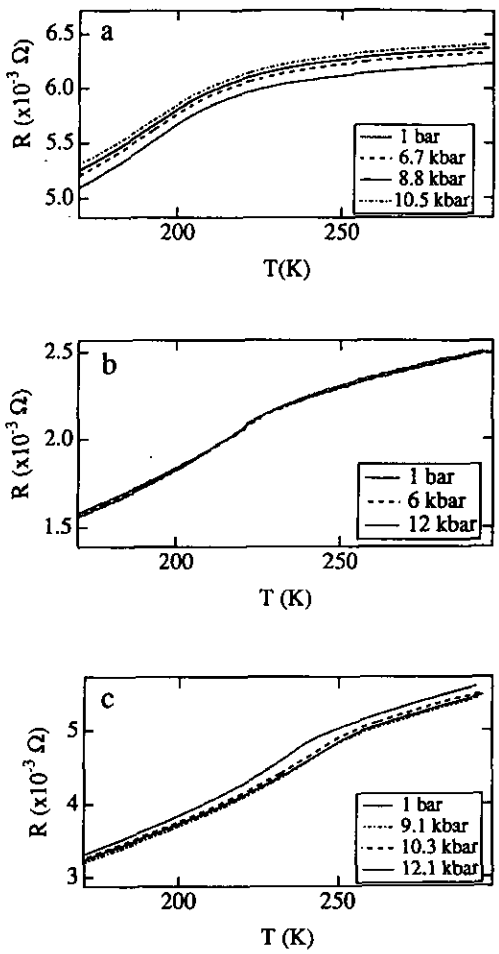

FIG. 14. Electrical resistance versus temperature under different applied pressures of samples $La_{1-x}Sr_xCoO_{3-\delta}$ with (a) x = 0.25, (b) x = 0.30, and (c) x = 0.45.

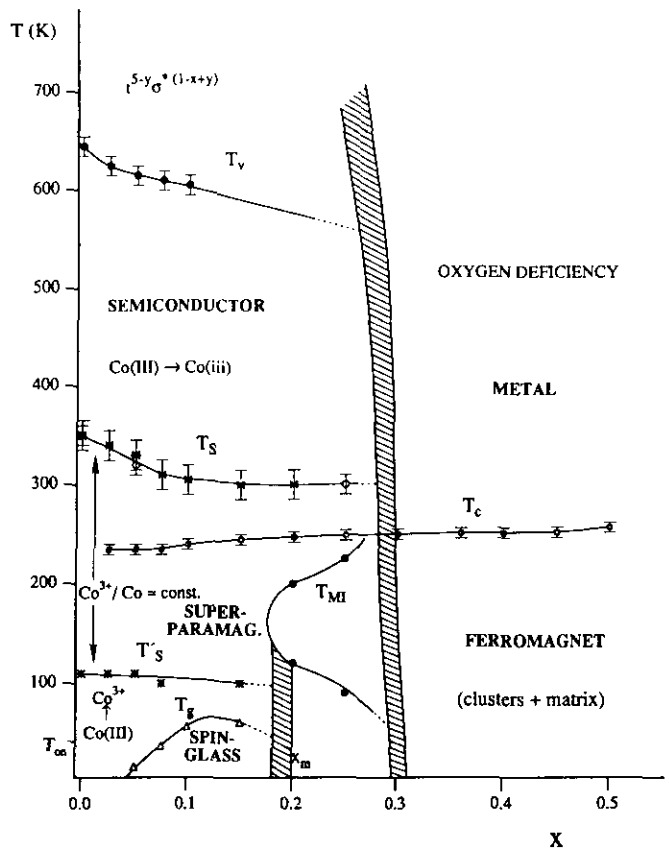

FIG. 15. Phase diagram of $La_{1-x}Sr_xCoO_{3-\delta}$ ($0 \leq x \leq 0.50$).

$t_2^5\sigma^{*1}$ while the high-spin Co^{3+}: $t_2^4e^2$ configuration evolve toward Co^{3+}: $t_2^4\sigma^{*2}$ configurations.

(5) At high temperatures, $T > 650$ K, the electrons of the narrow σ^* band retain their spin density parallel to the majority spin of the fluctuating local t_2^n configurations, and strong electron-lattice as well as spin-disorder scattering create a charge-carrier mobility that is at the crossover from small-polaron to itinerant-electron behavior; the χ_m^{-1} versus T curves again show a Curie–Weiss dependence, and the transport properties approach those of a poor metal.

The other limiting composition in Fig. 15, $La_{0.5}Sr_{0.5}CoO_{3-\delta}$ is a metallic ferromagnet; it has been interpreted (17) to represent the intermediate-spin configuration Co(iii/iv): $t_2^5\sigma^{*(0.5+2\delta)}$. Itoh *et al.* (19) include the $x = 0.50$ composition within the region where ferromagnetic hole-rich regions coexist with a hole-pool matrix; they refer to this region of the diagram as a magnetic "cluster-glass" phase field.

Interpretation of Fig. 15 requires an analysis of how the properties found for $LaCoO_3$ evolve with Sr doping to those exhibited by $La_{0.5}Sr_{0.5}CoO_{3-\delta}$.

The evoution of physical properties from $LaCoO_3$ to $La_{0.5}Sr_{0.5}CoO_{3-\delta}$ may be separated into two distinguishable compositional ranges separated by x_m.

(1) $0 < x < x_m$. Substitution of Sr^{2+} for La^{3+} oxidizes the CoO_3 array; for $x \leq 0.050$ the holes initially introduced create, formally, low-spin Co(IV): $t_2^5e^0$ configurations within a strongly covalent CoO_3 octahedral site complex. Since the neighboring trivalent cobalt are poised at a low-spin to high-spin transition, polarization of the O-$2p_\sigma$ electrons of the complex toward the Co(IV) ions stabilizes high-spin Co^{3+} ions on the opposite side of the oxygen atoms down to lowest temperatures. Thus, the holes trapped at isolated Sr^{2+} ions give rise to the formation of Co(IV).6 Co^{3+} clusters. Similar cooperative displacements of the oxygen in the Co–O–Co bond are responsible for stabilizing a nearly 50 : 50 high-spin : low-spin population in the $LaCoO_3$ matrix in the interval $T'_s < T < T_s$. For $x = 0.025$ and 0.050, the μ_{eff} obtained from a Curie–Weiss behavior of χ_m^{-1} (T) in the range $T_c < T < 350$ K provides a measure of the relative proportion of Co^{3+} and Co(III) ions coexisting with low-spin Co(IV) in this temperature interval since x = [Co(IV)] is known. For a material containing isolated Sr^{2+} ions forming Co(IV).6 Co^{3+} clusters in a $LaCoO_3$ matrix, the Co spin-state distribution is

$$x[\text{Co(IV)} + 6\ \text{Co}^{3+}] + y\ \text{Co}^{3+} + (1 - y - 7x)\ \text{Co(III)}.$$

By analogy with the parent $LaCoO_3$ the high-spin fraction in the temperature interval $110 < T < 350$ K should be $(y + 6x) \leq 0.5$ (12). From the measured slope of the χ_m^{-1} vs T curve in this interval, high-spin fractions of 0.40 for $x = 0.025$ and 0.42 for $x = 0.050$ are obtained for a spin-only contribution of the Co ions to the μ_{eff}.

With increasing x, the fraction of isolated Sr^{2+} ions with trapped Co(IV).6 Co^{3+} clusters at lowest temperatures decreases while larger clusters containing more than one Co(IV) are formed. Within these larger clusters, the covalent bonding would be strong enough to create molecular orbital (MO) σ^* states. Nevertheless, at the interface of the hole-rich clusters and the $LaCoO_3$ matrix, high-spin Co^{3+} ions are stabilized.

Inside the hole-rich regions, ferromagnetic coupling through Co^{3+}–O–Co(IV) superexchange interactions, or by double-exchange interactions of localized t_2 configurations via itinerant σ^* electrons, gives rise to the superparamagnetic behavior observed below T_c (26). Also, the ferromagnetic Curie temperature T_c of the clusters increases only slightly with increasing size of the clusters; it does not differ much from that of samples with $x > x_m$.

Furthermore, the hole-rich regions stabilize high-spin Co^{3+} ions at the interface to the hole-poor regions, and the magnetic coupling between superparamagnetic regions is antiferromagnetic via superexchange interactions between the high-spin Co^{3+} ions. Since the superparamag-

netic clusters are distributed randomly, frustration in the intercluster exchange interactions leads to noncollinear orientations of the cluster moments and a huge anisotropy below a magnetic blocking temperature T_g. Although ferromagnetic alignment of the superparamagnetic regions was improved by cooling in a magnetic field, full magnetic alignment below T_g is never achieved even in an applied field of 50 kOe (Fig. 2) because such an alignment would need to overcome the antiferromagnetic intercluster superexchange interactions. Since the distance between ferromagnetic clusters decreases as x gets bigger, the temperature T_g increases. We speculate that a Brillouin temperature dependence of the magnetization within a superparamagnetic cluster is responsible for the shoulder in the $\chi_m(T)$ curves of Fig. 1 near 150 K $> T_g$.

At lowest temperatures, the holes remain trapped in the superparamagnetic clusters and there are few charge carriers mobile at long range to contribute to either the electrical conductivity or the thermoelectric power. As the temperature rises, the concentration of Co^{3+} ions in the matrix increases and α increases to a large positive value (300 μV/K for $x = 0.025$, Fig. 8), where it remains temperature-independent over the interval $T_s' < T < T_s$. This behavior, which contrasts witih the parent compound $LaCoO_3$ only in the lack of any measurable $d\alpha/dT$ in the latter interval, signals a nearly constant concentration p of mobile small-polaron holes in the doped samples $0 < x < x_m$. Equation [3] gives a $\Delta H_m + (1/2)\,\Delta H_t \approx 0.08$ eV and a motional enthalpy of the small polarons, $\Delta H_m < 0.04$ eV.

These data indicate that the trapping energy ΔH_t decreases not only with increasing x, but also with increasing temperature. Moreover, as the ratio of dynamically fluctuating high-spin and low-spin cobalt ions in the matrix approaches 50 : 50 in the interval $T_s' < T < T_s$, essentially all the holes move freely. A hole released from a Sr^{2+} ion trap moves in the matrix as a Co(IV).6 Co^{3+} cluster, i.e., it remains a "dressed" polaron that moves with an activated mobility, so the Seebeck coefficient is temperature-independent in the interval $T_s' < T < T_s$, where the concentration of mobile holes per cobalt is $c \approx x$.

As illustrated in Fig. 16, a dynamic short-range ordering of high-spin and low-spin cobalt ions allows a hole to move as a low-spin Co(IV) ion on the low-spin subarray while the localized e electrons only fluctuate from one cobalt to another. In a configuration fluctuation, the Co(III) ions transfer two t_2 electrons equally to each of six neighboring Co^{3+} ions and a Co^{3+} ion transfers back two e electrons equally to each of six neighboring Co(III) ions, to give no net transfer of charge but an interchange of spin states. In this situation, a Co(IV) on the low-spin array only transfers a single t_2 electron to its neighbors; the missing t_2 electron becomes condensed as a t_2 hole

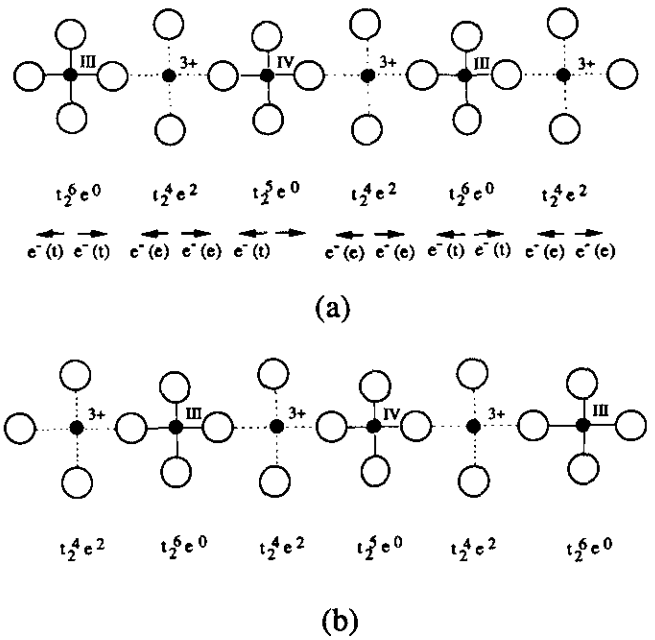

FIG. 16. Schematic representation of hole transfer on the low-spin subarray for dynamic ordering of high-spin and low-spin cobalt ions. In the picture the big open circles represent oxygen ions, while the smaller solid circles correspond to cobalt ions. (a) initial configurations. (b) new situation after transfer of the hole.

on one of the neighboring cobalt centers that has undergone an interchange from a high-spin to a low-spin state. Thus in the interval $T_s' < T < T_s$ a small-polaron t_2 hole is mobile at long range while remaining within the low-spin array.

At higher temperatures $T_s < T < T_v$, the progressive transformation of low-spin Co(III) to intermediate-spin Co(iii) takes place in the trivalent cobalt matrix as in the parent $LaCoO_3$, so we extend the T_v line in Fig. 15 to x_m. Since the spin state of the intercluster matrix is changing in that temperature range, it is only above T_v that a meaningful value of μ_{eff} can be obtained in the compositional range $0 \leq x \leq 0.15$ from a high-temperature Curie–Weiss fit to the χ_m^{-1} vs T plot. These fits give the μ_{eff} values plotted in Fig. 4; they indicate an increasing ratio of Co(iii) to Co^{3+} ions, from 1.5 to 5.0, with increasing x over the interval $0.075 \leq x \leq 0.15$, which means that y decreases with increasing x in the high-temperature configuration $t_2^{(5-y)}\sigma^{*(1-x+y)}$.

On the other hand, the progressive transformation of the Co(III) on the low-spin array to Co(iii) : $t_2^5e^1$ in the interval $T_s < T < T_v$ allows interaction between neighboring e electrons and lowers the difference in e electron potential energy at the two subarrays. The result is a transformation from localized e electrons at Co^{3+} ions to extended σ^* electrons; these may evolve from molecular orbitals of a cluster to itinerant-electron orbitals of a nar-

row σ^* band. The σ^* electron density remains parallel to the local majority spin of the t_2 manifold and is greater at high-spin than intermediate-spin ions. At temperatures $T > T_v$, a partially filled σ_α^* band (the subscript α refers to the majority spin configuration) (see Fig. 17b) reflects a lifting of the local spin degeneracy by intraatomic exchange; the resulting e holes contribute a dominating transport term to the Seebeck coefficient while sharply lowering the resistance of the compound (Figs. 8 and 11). Consequently, the magnitude of the Seebeck coefficient decreases from 300 μV/K at 330 K to a low value at $T > 650$ K. Since oxidation enhances the covalent mixing between Co-e and O-$2p_\sigma$ orbitals, an increase in x favors transformation of the localized e electrons to extended σ^* electrons (26). The result is a lowering of both T_v and T_s with increasing x.

It is worth emphasizing here that the phase segregation takes place in the mixed-valent material upon doping, a segregation into hole-rich superparamagnetic regions separated by a hole-poor matrix similar to $LaCoO_3$. Phase segregation implies the existence of two distinguishable thermodynamic states, the parent phase and a hole-rich ferromagnetic phase. The existence of two distinguishable electronic states within the same crystallographic phase is found in a few mixed-valent perovskite systems where the equilibrium metal–oxygen bond length can be double-valued; the longer bond length corresponds to a more ionic bond, the shorter one to a more covalent bond. In single-valent $NdNiO_3$, for example, the double-valued bond length manifests itself as a first-order contraction on increasing the temperature through T_N where an insulator–metal transition accompanies the loss of long-range antiferromagnetic order (27). In the cuprate superconductor $La_2CuO_{4+\delta}$, a spinodal transition segregates an oxygen-rich superconductive phase from the antiferromagnetic parent phase (28). In $La_{1-x}Sr_xCoO_{3-\delta}$ the magnetic data show clearly that a phase segregation occurs. Since phase segregation would occur at a temperature $T < T_v \leq 650$ K, where the Sr^{2+} ions are inmobile, any spinodal phase segregation cannot be induced by a conventional diffusion process; however, it can be stabilized by cooperative atomic displacements in a manner similar to that postulated for underdoped $La_{2-x}Sr_xCuO_4$ (29).

(2) $x_m < x < 0.50$. For $x > x_m$ a ferromagnetic state is established below T_c (13–16). At $x_m \approx 0.20$, the ferromagnetic clusters reach a magnetic percolation threshold; the ferromagnetism is confined to a region that percolates continuously throughout the volume while leaving a second interconnected network of matrix in which Co(III) ions are converted to Co^{3+} and Co(iii) spin states with increasing temperature, as in $LaCoO_3$. Once the intercluster percolation threshold has been reached, an apparent ferromagnetic saturation is more easily approached at any given temperature for $0.20 \leq x \leq 0.50$, Fig. 6. Nevertheless, the χ_m curves of Fig. 5b indicate that in an $H = 20$ Oe, some superparamagnetic clusters remain isolated; transformation of some high-spin to low-spin configurations is also occurring below 110 K at trivalent cobalt within the matrix between ferromagnetic regions. Moreover, Fig. 6 shows almost saturation in a field of 50 kOe at 5 K, but very low remanence after removal of the field; this behavior indicates the presence of a substantial volume in which reversible magnetization processes occur. Thus the mixture of ferromagnetic and matrix regions within the same crystallographic phase gives rise to peculiar ferromagnetic properties; Itoh *et al.* (19) have found others and referred to them as magnetic "cluster-glass" behavior. Our experiments confirm that the peculiar magnetic behavior extends to $x = 0.50$, which implies that magnetic heterogeneity persists to the $x = 0.50$ composition. The Mössbauer data of Bahadur *et al.* (18) also confirm the presence of magnetic and nonmagnetic regions. In the transitional range $0.20 \leq x \leq 0.30$, the magnetic interactions percolate throughout the volume, but metallic conduction is only established in a narrow temperature range within the interval $100 < T < T_c$; with increasing temperature below T_c, an increasing spin-disorder scattering introduces a metallic temperature dependence to $R(T)$ (Fig. 13), but below 100 K, which is close to T_s' for the matrix, the increasing population of low-spin Co(III) in the matrix reestablishes a semiconductive temperature dependence. The result is a peculiar shape of the semiconductor–metal transition temperature T_{MI} in Fig. 15. In the range $0.30 < x < 0.50$ the ferromagnetic regions percolate conductively as well as magnetically, and the metallic conductivity of these regions is fully manifest. Thus, we conclude that the hole-rich regions of the superparamagnetic clusters at $x < x_m$ are metallic with a spin configuration close to $t_2^5\sigma^{*0.5}$.

The contribution of the Sr-poor matrix to the Seebeck coefficient can be clearly seen in the $\alpha(T)$ curves of Fig. 9. In the materials without large ferromagnetic clusters, $\alpha(T)$ has an important positive value in the temperature range 110 K $< T <$ 350 K (Fig. 7). The domains of interconnected ferromagnetic clusters give a negative contribution to $\alpha(T)$ that increases with x relative to the positive contribution to $\alpha(T)$ from the matrix (Fig. 9). It would appear that the contribution to $\alpha(T)$ from the matrix between the ferromagnetic regions remains dominant for $x = 0.20$ and $x = 0.25$.

Above $T_c \approx 240 \pm 10$ K, spin-disorder scattering in the metallic regions reduces the conductivity of the ferromagnetic domains whereas the conductivity of the matrix increases with T in the range where Co(iii) ions are being created, which is 350 K $< T <$ 650 K in $LaCoO_3$ and appears to drop to 300 K $< T <$ 600 K by $x = 0.25$. It follows that the maximum contribution to $\alpha(T)$ from the matrix may be observed for $T > T_c$. Thus, the decrease

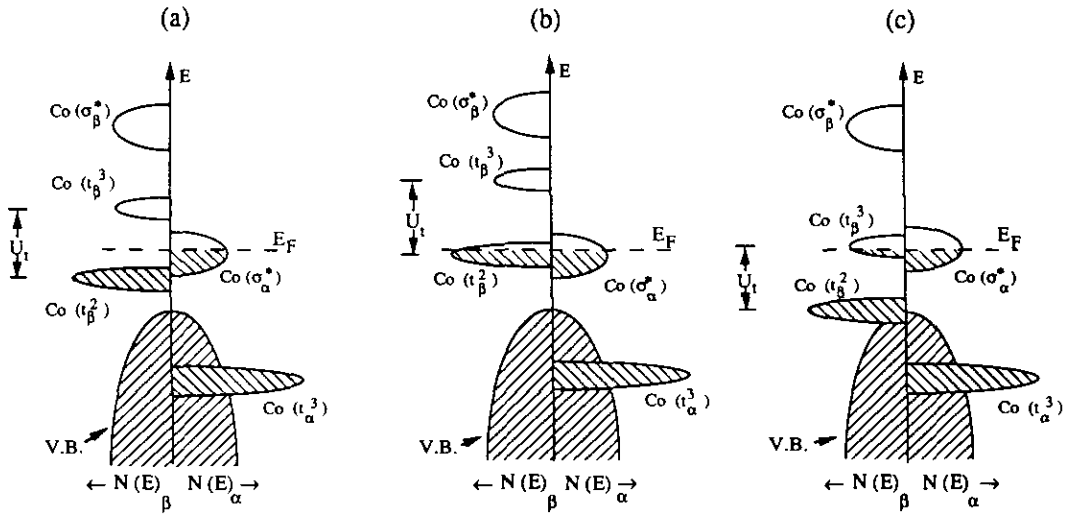

FIG. 17. Schematic representation of the electronic structure of $La_{1-x}Sr_xCoO_{3-\delta}$ ($x \geq x_m$). (a) Situation corresponding to a purely intermediate-spin configuration $t_2^5\sigma^{*(1-x+2\delta)}$. This situation is present below 300 K within the metallic, ferromagnetic clusters and, in high magnetic fields, in the entire material. (b) Situation at higher temperatures, where the material is evolving toward a higher-spin configuration $t_2^{5y}\sigma^{*(1-x+y+2\delta)}$ ($y > 0$); it also applies to $T \geq T_v$ for $0 \leq x < x_m$. (c) Situation at lower temperatures or higher pressures, where low-spin Co(III) ions are present in the matrix.

in $\alpha(T)$ with increasing $T > 300$ K for $x = 0.25$ (Fig. 10) is consistent with that for $T > 350$ K for $x = 0.025$ (Fig. 8).

At higher temperatures, the distinction between matrix and ferromagnetic regions becomes blurred; in both, the e electrons are transformed into σ^* electrons, and we may think in terms of an average spin configuration $t_2^{(5-y)}\sigma^{*(1-x+y+\delta)}$ where y decreases and δ increases with increasing x. For discussion, we illustrate first a mean electron energy diagram in Fig. 17a for a $t_2^5\sigma^{*(1-x+2\delta)}$ situation ($y = 0$). Localized t_2-electron spin configurations remove the spin degeneracies and introduce a correlation splitting U_t between the filled t_β^2 and the empty t_β^3 configurations. In this case the Fermi energy in the partially filled σ_α^* band lies between the t_β^2 and t_β^3 energies. Creation of some high-spin Co^{3+} may shift E_F down into the t_β^2 energy band ($y > 0$) (Fig. 17b). At lower temperatures, creation of low-spin Co(III) in the matrix may shift E_F up into the t_β^3 energy level (Fig. 17c). Such movements of E_F will have associated with them a transfer of some spectral weight into the Hubbard gap from the respective t_β^n energy levels; this transfer appropriate to Co^{3+} and Co(III) configurations is not shown in Figs. 17b and 17c. With this energy diagram, we check the spin state of the ferromagnetic regions.

In an intermediate-spin configuration $t_2^5\sigma^{*(1-x+2\delta)}$ at each cobalt (Fig. 17a), for the system $La_{1-x}Sr_xCoO_{3-\delta}$, the spin-only ferromagnetic moment per cobalt would be

$$\mu_{Co} = (1.5 + 2\delta)\mu_B.$$

To this would be added an orbital contribution from the minority-spin t_2 electrons. In a heterogeneous mixture of ferromagnetic hole-rich regions and trivalent-cobalt hole-poor matrix, it is necessary to stabilize the matrix in its intermediate-spin state to low temperatures to achieve this value of μ_{Co}. We may do this by applying a large magnetic field H. If a large H transforms the matrix to an intermediate-spin state coupled ferromagnetically to the ferromagnetic regions, then extrapolation of the $M(H)$ curves from high-fields to $H = 0$ would allow a check on the predicted value for μ_{Co}. We assume this to be the case for $H = 50$ kOe, a shift of E_F into the t_β^3 energy as indicated in Fig. 17c setting in only at much lower values of H to contribute to the relatively low remanence (Fig. 6). With this procedure, the measured μ_{Co} are found to agree well with prediction for $x = 0.45$ and 0.50. A $\mu_{Co} = 1.9$ μB has been reported by Itoh *et al.* (19) for $x = 0.50$.

We comment here on the difficulty to obtain oxygen stoichiometry with higher Sr contents. We believe it reflects the change in compressive stress on the Co–O bonds due to bond-length mismatch. In an ABO_3 perovskite, a measure of the bond-length mismatch is the tolerance factor

$$t = (A\text{–O})/\sqrt{2}(B\text{–O}),$$

where A–O and B–O are the equilibrium bond lengths. A $t < 1$ places the A–O bonds under tension and the B–O bonds under compression. It has been observed (28) that the high-T_c copper oxides can be doped p-type, but not n-type, where the Cu–O bonds are under compression; n-type, but not p-type, where the Cu–O bonds are

under tension. Removal of antibonding electrons from a B–O bond relieves a compressive stress; addition of an antibonding electron relieves a tensile stress. A $t < 1$ in $LaCoO_3$ facilitates oxidation of the CoO_3 array. However, substitution of a larger Sr^{2+} ion and oxidation of the CoO_3 array increases t until the compressive stress on the CoO_3 array is gone at larger x. By $x = 0.50$, a high oxygen pressure is needed to obtain stoichiometric $La_{0.5}Sr_{0.5}CoO_3$.

The application of pressure can also shift the Fermi energy E_F relative to the energies t_β^2 and t_β^3. Pressure would favor stabilization of low-spin Co(III) ions in the matrix, thus raising E_F into the t_β^3 level; it would also broaden the σ_α^* band. The $x = 0.25$ sample is in the transition region for establishing conductive percolation pathways throughout the volume; the resistance in this case should increase with the stabilization of more Co(III) in the matrix despite any increase in the σ_α^* bandwidth within the hole-rich regions. Consistent with this interpretation is a $dR/dP > 0$ for all temperatures $T < 300$ K. In the $x = 0.45$ sample, where the percolation pathways are well-established, the electrical conductivity is dominated by the metallic, ferromagnetic regions. In this compound a $dR/dP < 0$ reflects a broadening of the σ_α^* bands. A small increase in R at $P = 10.3$ kbar may be due to the creation of low-spin Co(III) ions in the matrix that scatter the σ_α^* electrons. In the case of $x = 0.30$, the opposing effects cancel out.

CONCLUSIONS

Magnetic and transport data for the system $La_{1-x}Sr_xCoO_{3-\delta}$ ($0 \leq x \leq 0.50$) have led to the preliminary-phase diagram shown in Fig. 15. An oxygen parameter $\delta = 0$ is found only for $0 \leq x < 0.30$; at room temperature, it increases with x to $\delta \approx 0.06$ at $x = 0.50$ in the range $0.30 \leq x \leq 0.50$ with further oxygen loss at higher temperatures. The diagram contains several critical parameters:

x_m: a magnetic percolation threshold.

T_{on}: onset temperature for the conversion of low-spin Co(III) to higher spin states.

T_s' and T_s: lower and upper limits of a temperature interval in which short-range ordering of low-spin and high-spin cobalt stabilizes a nearly constant high-spin: low-spin ratio in the trivalent cobalt matrix.

T_v: critical temperature above which all localized e electrons at high-spin Co^{3+} are transformed to extended σ^* electrons.

T_c: ferromagnetic Curie temperature for an intermediate-spin configuration $t_2^5\sigma^{*(1-x+2\delta)}$ within superparamagnetic clusters ($x < x_m$) or within a magnetically percolating phase ($x > x_m$).

T_g: magnetic blocking temperature for superparamagnetic clusters.

T_{MI}: semiconductor–metal transition temperature.

Upon Sr doping, the material segregates into hole-rich, metallic ferromagnetic regions and a hole-poor matrix similar to $LaCoO_3$.

For very low Sr doping, the x holes introduced into the CoO_3 array are trapped at isolated Sr^{2+} ions as covalent $Co(IV)O_6$ centers. A resulting stabilization to $T = 0$ K of high-spin Co^{3+} ions on the opposite side of a center oxygen creates Co(IV).6 Co^{3+} clusters that become superparamagnetic below T_c.

With increasing x, the fraction of isolated Sr^{2+} ions with trapped Co(IV).6 Co^{3+} clusters at lowest temperatures decreases while larger clusters containing more than one hole are formed. Within these clusters the Co ions are stabilized in an intermediate-spin configuration $t_2^5\sigma^{*(1-x')}$, where $x' = xV/v \approx 0.5$ is the hole concentration in the hole-rich regions of volume v relative to total volume V of the samples. These hole-rich regions are ferromagnetic. For $x < x_m$ the clusters are isolated from one another and show superparamagnetic behavior below T_c. Long-range magnetic order via frustrated intercluster interactions occurs below a spin-blocking temperature T_g that increases with x.

In the $LaCoO_3$ matrix, a progressive change with increasing T from low-spin Co(III) to high-spin Co^{3+} in the interval $T_{on} < T < T_s'$ is arrested in the interval $T_s' < T < T_s$ by short-range ordering of high-spin and low-spin ions on alternate cobalt sites. In the interval $T_s' < T < T_s$, the holes move on the low-spin array as small polarons with a small motional enthalpy $\Delta H_m \leq 0.04$ eV. In the interval $T_s < T < T_v$, the remaining Co(III) are progressively transformed to intermediate-spin Co(iii) with an associated transformation of the localized e electrons at Co^{3+} ions to extended σ^* molecular and then band states. At $T > T_v$, the transformation to a homogeneous $t^{(5-y)}\sigma^{*(1+y-x)}$ configuration is complete. With increasing x, a greater covalent contribution to the Co–O σ bonding lowers T_s, T_v, and y.

A magnetic percolation threshold is reached at x_m, and for $x_m < x \leq 0.50$ the ferromagnetic hole-rich regions couple ferromagnetically to give bulk ferromagnetism below T_c. The electrical percolation threshold depends on the spin state of both the hole-rich and hole-poor regions. The temperature dependence of the spin state in the hole-poor regions modulates the metallic conduction in the magnetically percolating hole-rich regions in the transitional range $0.20 \leq x \leq 0.30$, and spin-disorder scattering in the hole-rich regions introduces an important temperature dependence to their resistance below T_c. The result is a reentrant semiconductor–metal transition temperature T_{MI} in the transitional range. Metallic ferromagnetism is found for the range $0.30 \leq x \leq 0.50$, but the presence of a hole-poor matrix interpenetrating the metallic, ferromagnetic regions per-

sists to $x = 0.50$. This interpretation of hole-rich and hole-poor phases gives rise to the peculiar magnetic behavior referred to by Itoh *et al.* (19) as a "cluster glass".

Application of high magnetic fields, $H > 25$ kOe, appears to be sufficient to retain to 5 K the trivalent cobalt of the matrix in an intermediate-spin state. The application of hydrostatic pressure, on the other hand, appears to increase the fraction of low-spin Co(III) in the matrix.

ACKNOWLEDGMENTS

The authors thank the Ministerio de Educación y Ciencia of Spain and the Fulbright Commission for the grant to M.A.S.R. and the Robert A. Welch Foundation of Houston, TX (Grant F-1066) and the National Science Foundation (Grant DMR-9223552) for the remaining support. J-S. Zhou is gratefully acknowledged for the high-pressure experiments, for all his experimental advice on transport measurements, and for helpful discussions.

REFERENCES

1. W. C. Koehler and E. O. Wollan, *J. Phys. Chem. Solids* **2,** 100 (1957).
2. R. R. Heikes, R. C. Miller, and R. Mazelsky, *Physica* **30,** 1600 (1964).
3. P. M. Raccah and J. B. Goodenough, *Phys. Rev.* **155,** 932 (1967).
4. N. Menyuk, K. Dwight, and P. M. Raccah, *J. Phys. Chem. Solids* **28,** 549 (1967).
5. G. Thornton, B. C. Tofield, and D. E. Williams, *Solid State Commun.* **44,** 1213 (1982).
6. V. G. Bhide, D. S. Rajoria, G. R. Rao, and C. N. R. Rao, *Phys. Rev. B* **6,** 1021 (1972).
7. G. Thornton, F. C. Morrison, S. Partington, B. C. Tofield, and D. E. Williams, *J. Phys. C Solid State Phys.* **21,** 2871 (1988).
8. K. Asai, P. Gehring, H. Chou, and G. Shirane, *Phys. Rev. B* **40**(16), 10982 (1989).
9. T. Arunarkavalli, G. U. Kulkarni, and C. N. R. Rao, *J. Solid State Chem.* **107,** 299 (1993).
10. M. Abbate, J. C. Fuggle, A. Fujimori, L. H. Tjeng, C. T. Chen, R. Potze, G. A. Sawatzky, H. Eisaki, and S. Uchida, *Phys. Rev. B* **47,** 16124 (1993).
11. S. R. Barman and D. D. Sarma, *Phys. Rev. B* **49,** 13979 (1994).
12. M. A. Señarís-Rodríguez and J. B. Goodenough, *J. Solid State Chem.* **116,** 224 (1995).
13. G. H. Jonker and J. H. van Santen, *Physica* **19,** 120 (1953).
14. P. M. Raccah and J. B. Goodenough, *J. Appl. Phys.* **39**(2), 1209 (1968).
15. V. G. Bhide, D. S. Rajoria, C. N. R. Rao, G. Rama Rao, and V. G. Jadhao, *Phys. Rev. B* **12** (1975).
16. C. N. R. Rao, O. M. Parkash, D. Bahadur, P. Ganguly, and S. Nagabhushana, *J. Solid State Chem.* **22,** 353 (1977).
17. J. B. Goodenough, *Mater. Res. Bull.* **6,** 967 (1971).
18. D. Bahadur, S. Kollali, C. N. R. Rao, M. J. Patni, and C. M. Srivastava, *J. Phys. Chem. Solids* **40,** 981 (1979).
19. M. Itoh, I. Natori, S. Kubota, and K. Motoya, *J. Phys. Soc. Jpn.* **63,** 1486 (1994).
20. K. Asai, O. Yokokura, N. Nishimori, H. Chou, J. M. Tranquada, G. Shirane, S. Higuchi, Y. Okajima, and K. Kohn, *Phys. Rev. B* **50,** 3025 (1994).
21. J. B. Goodenough, J-S. Zhou, and J. Chan, *Phys. Rev. B* **47,** 5275 (1993).
22. J. D. Thompson, *Rev. Sci. Instrum.* **55,** 231 (1984).
23. J. A. Mydosh, *in* "Spin Glasses. An Experimental Introduction." Taylor & Francis, London (1993).
24. N. Menyuk, P. M. Raccah, and K. Dwight, *Phys. Rev.* **166,** 510 (1968).
25. D. S. Chapin, J. A. Kafalas, and J. M. Honig, *J. Phys. Chem.* **69,** 1402 (1965).
26. J. B. Goodenough, *Prog. Solid State Chem.* **5,** 145 (1971).
27. J. B. Torrance, P. Lacorre, D. I. Nazzal, E. J. Ansaldo, and Ch. Niedermayer, *Phys. Rev. B* **45,** 8209 (1992).
28. J. B. Goodenough, J-S. Zhou, and K. Allan, *J. Mater. Chem.* **1,** 715 (1991).
29. J. B. Goodenough, J-S. Zhou, and J. Chan, *Phys. Rev. B* **47,** 5275 (1993).